PHYSICAL REVIEW E **100**, 041201(R) (2019)

Rapid Communications

Three-dimensional particle-in-cell modeling of parametric instabilities near the quarter-critical density in plasmas

H. Wen,[1,2] A. V. Maximov,[1,2] R. Yan,[1,2,*] J. Li,[1,2,†] C. Ren,[1,2,3] and F. S. Tsung[4]
[1]Laboratory for Laser Energetics, University of Rochester, Rochester, New York 14623-1299, USA
[2]Department of Mechanical Engineering, University of Rochester, Rochester, New York 14627, USA
[3]Department of Physics and Astronomy, University of Rochester, Rochester, New York 14627, USA
[4]Department of Physics and Astronomy, University of California Los Angeles, Los Angeles, California 90095, USA

(Received 17 April 2019; published 4 October 2019)

The nonlinear regime of laser-plasma interactions including both two-plasmon decay (TPD) and stimulated Raman scattering (SRS) instabilities has been studied in three-dimensional (3D) particle-in-cell simulations with parameters relevant to the inertial confinement fusion (ICF) experiments. SRS and TPD develop in the same region in plasmas, and the generation of fast electrons can be described accurately with only the full model including both SRS and TPD. The growth of instabilities in the linear stage is found to be in good agreement with analytical theories. In the saturation stage the low-frequency density perturbations driven by the daughter waves of the SRS side scattering can saturate the TPD and consequently inhibit the fast-electron generation. The fast-electron flux in 3D modeling is up to an order of magnitude smaller than previously reported in 2D TPD simulations, bringing it close to the results of ICF experiments.

DOI: 10.1103/PhysRevE.100.041201

Since the 1960's, the pursuit of inertial confinement fusion (ICF) driven by lasers has led to large-scale research on laser interactions with the plasmas of ICF targets [1]. Decades of laser-plasma interaction (LPI) research [2] have concentrated on several processes in laser-produced plasmas that can grow as parametric instabilities at high-enough laser intensities, namely, stimulated Raman scattering (SRS), stimulated Brillouin scattering (SBS), and two-plasmon decay (TPD).

Laser light can propagate in a plasma up to the critical density (n_c) determined by the laser frequency. The region near quarter-critical density ($\frac{1}{4}n_\mathrm{c}$) is a possible place for the interplay between SRS, SBS, and TPD as all three instabilities can develop at that region. Plasmons produced by SRS and TPD generate fast electrons that can preheat the fusion fuel and degrade the performance of the ICF targets [1], making LPIs a concern in ICF experiments. Several mechanisms of fast-electron acceleration have been studied before, namely, staged acceleration [3,4], Langmuir cavitation [5,6], and wave breaking [7].

In this Rapid Communication, LPI is studied using particle-in-cell (PIC) modeling [8], which can describe the interplay between different instabilities and the particle distributions including fast-electron generation. Usually, few hot electrons are found in the simulations at the linear stage of the TPD and SRS instabilities. The electron acceleration becomes effective after the instabilities saturate [4].

The TPD-related waves are mostly localized in the plane of polarization [9], which is defined by the incident laser wave vector (in the x direction) and the laser electric field vector (in the y direction). The SRS side scattering develops mostly outside of the polarization plane, and its scattered-light wave vector is almost perpendicular to the incident laser wave vector [10,11]. Scattered light waves can also propagate in the direction parallel or antiparallel to the laser wave vector (forward- and backscattering, respectively) [12]. A two-dimensional (2D) simulation in the polarization plane (x-y) or in the perpendicular plane (x-z) will be referred to as p polarized (PP) or s polarized (SP), respectively. Two-dimensional simulations can model only the interaction where either (in PP) TPD or (in SP) SRS dominates except for the high-frequency hybrid instability (HFHI) [13] case when the SRS scattered light propagates in the backward direction and the SRS-related and TPD-related waves are in the same (x-y) plane. The three-dimensional (3D) simulations are required to study the interaction including both TPD and SRS. In this Rapid Communication, the results of several 3D simulations for different plasma parameters and incident laser profiles are presented and compared with the respective 2D simulations to illustrate that both TPD and SRS strongly influence the LPI near $\frac{1}{4}n_\mathrm{c}$. In the 3D modeling including both TPD and SRS the fast-electron flux is reduced by up to an order of magnitude compared to 2D TPD simulation results published before [4].

Here, we describe in detail a 3D simulation for the parameters relevant to ICF experiments [14,15]. A CH plasma is initialized with the electron temperature $T_\mathrm{e} = 2$ keV, and the temperatures for both ion species $T_\mathrm{i} = 1$ keV. The incident laser beam with intensity $I = 9 \times 10^{14}$ W/cm^2 propagates in the direction of density inhomogeneity (x). A linear density profile with the scale length $L = 100$ μm is assumed at the initial time. The size of the simulation box is 21 μm × 8.4 μm × 6.7 μm modeling the density range from $0.21n_\mathrm{c}$ to $0.26n_\mathrm{c}$.

---

[*] Present address: University of Science and Technology of China, Hefei, Anhui 230026, China.

[†] Present address: University of California, San Diego, CA 92093, USA.

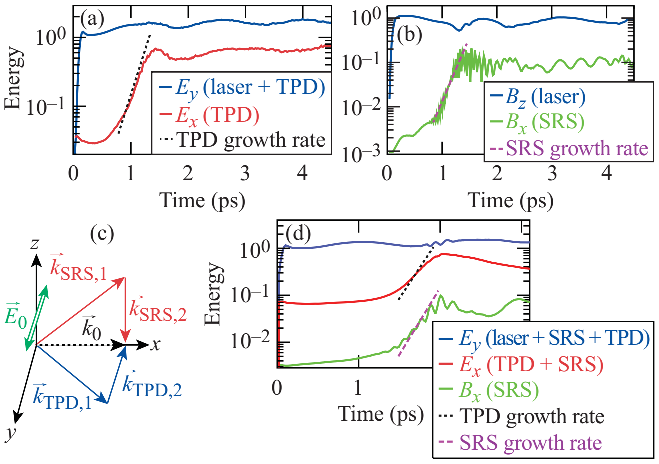

FIG. 1. The integrated energy of different field components in the simulation region as a function of time for the (a) 2D p-polarized simulation, (b) 2D s-polarized simulation, and (d) 3D simulation. The wave-vector diagram for TPD and SRS is shown in (c).

Two 2D simulations (PP and SP) with the same physical parameters were also performed. The TPD threshold parameter η [9] is 1.9 ($\eta = 1$ at threshold), and the SRS backscattering threshold parameter N [12] is 0.5 ($N = 0.26$ at threshold) for these simulations. The SRS side-scattering threshold [10,11] is close to the backscattering threshold. Both absolute TPD and absolute SRS instabilities are expected to grow. The threshold of the convective SRS [10] is not exceeded for the parameters described above. The time evolution of the energy of the field components in the simulation region is shown in Fig. 1. The field energy is defined as the square of the electric or magnetic field amplitudes integrated over the simulation region normalized to the respective laser field energy at an early time (when there are no instabilities). In 2D PP [Fig. 1(a)], the E_x field contains most of the energy of the TPD plasmons with a larger wave vector. One can see that the field energy associated with the TPD instability stays at about the same level (close to 70% of the energy of the incident laser electric field) after 2.5 ps, when one can assume that the saturation stage is reached. In 2D SP, the energy of the B_x field [Fig. 1(b)] is used as an indicator for the level of SRS instability. The energy of the scattered light saturates at a level of about 8% of the energy of the incident laser magnetic field.

In the 3D simulation, the diagram for TPD and SRS is shown in Fig. 1(c), where the incident light ($\vec{k}_0$) decays into a plasmon ($\vec{k}_{\mathrm{SRS},1}$) and a light wave ($\vec{k}_{\mathrm{SRS},2}$) in the case of SRS and into two plasmons ($\vec{k}_{\mathrm{TPD},1}$ and $\vec{k}_{\mathrm{TPD},2}$) in the case of TPD. The E_x field energy [red line in Fig. 1(d)] now includes the energy of the TPD plasmons and the SRS plasmons. The red line is overlaid with the dotted black line that represents the maximum TPD growth rate [9] ($7.7 \times 10^{-4}\omega_0$) minus the damping rate of plasma waves ($2.1 \times 10^{-4}\omega_0$) measured in the 3D simulation. The E_x field saturates at a level of about 40% of the laser field energy, which is much lower than the saturation level in 2D PP. The green line in Fig. 1(d) corresponds to the energy of the scattered light wave (propagating in the z direction) from the SRS and is overlaid with the dashed purple line representing the maximum growth rate of the SRS [10] ($8.2 \times 10^{-4}\omega_0$) minus the damping rate of the plasma waves. One can see from Fig. 1(d) that the growth of the B_x field energy in time is in reasonable agreement with the theoretical result [10]. The B_x field energy is under 10% of the incident laser field energy after reaching its peak value, which is consistent with the 2D SP result.

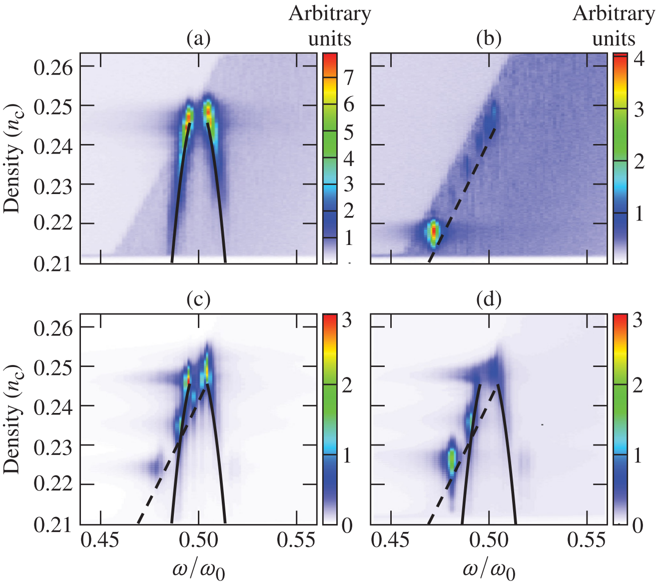

FIG. 2. (a) Plasma-wave spectra in the linear instability stage as a function of plasma density and the wave frequency normalized to laser frequency in 2D PP, (b) 2D SP, and (c) 3D simulation for modes with $0 \leqslant k_z/k_0 < 0.2$ and (d) $0.2 \leqslant k_z/k_0 < 3$. The overlaid solid black lines and the dashed black lines represent the dispersion relations satisfying the matching conditions for TPD and SRS, respectively.

The spectra of plasma waves ($|\vec{E}_{\mathrm{L}}|$) obtained at a time interval between 0.3 and 1.0 ps in the 2D PP and SP simulations are plotted in Figs. 2(a) and 2(b), respectively. From the 3D simulation, the spectra of plasma waves at a time interval between 1.3 and 2.0 ps are plotted in Fig. 2(c) (close to the $k_z = 0$ plane, where TPD dominates) and in Fig. 2(d) (far away from the $k_z = 0$ plane, where SRS dominates). One can see from Figs. 2(c) and 2(d) that TPD and SRS coexist near $\frac{1}{4}n_{\mathrm{c}}$. The spectra of the unstable modes for TPD and SRS are close to the linear theory results (see overlaid lines in Fig. 2).

As the instability evolves from the linear stage to the saturation stage, the frequency spectra shown in Fig. 2 evolve into the spectra shown in Fig. 3. One can see that the spectra in all these simulations are broader in the saturation stage compared to the linear stage. The density in Fig. 3 is calculated using the initial density profile. Compared to 2D PP [Fig. 3(a)], the TPD is much weaker at densities lower than $0.23n_{\mathrm{c}}$ in the 3D simulation [Fig. 3(c)]. The weakening of the TPD modes at these densities is also illustrated in Fig. 4(a) [and Fig. 4(b)], where the spectrum of plasma waves at densities below $0.23n_{\mathrm{c}}$ in the saturation stage is integrated over k_z (and k_y). There are no prominent modes along the TPD hyperbola [16] [black solid line in Fig. 4(a)] at $k_x > k_0$, which corresponds to the TPD daughter waves with larger wave

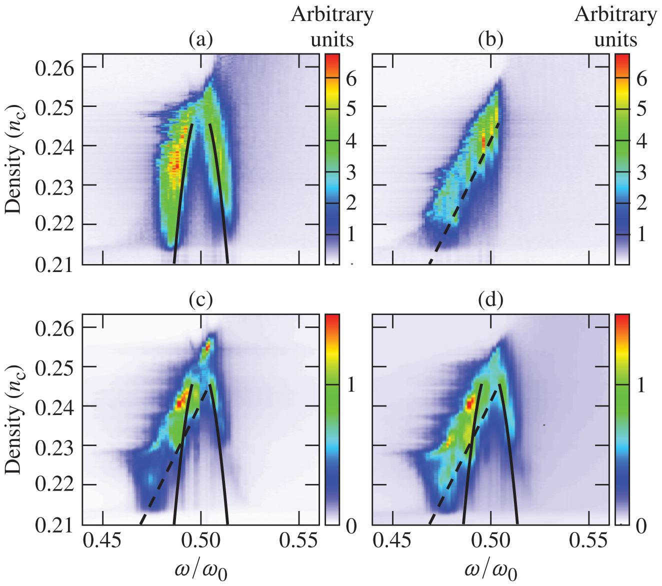

FIG. 3. Plasma-wave spectra in the saturation stage in the 2D (from 3.3 to 4.1 ps) and 3D (from 2.3 to 3.1 ps) simulations as a function of plasma density and the wave frequency. Each panel displays the same quantity as in Fig. 2.

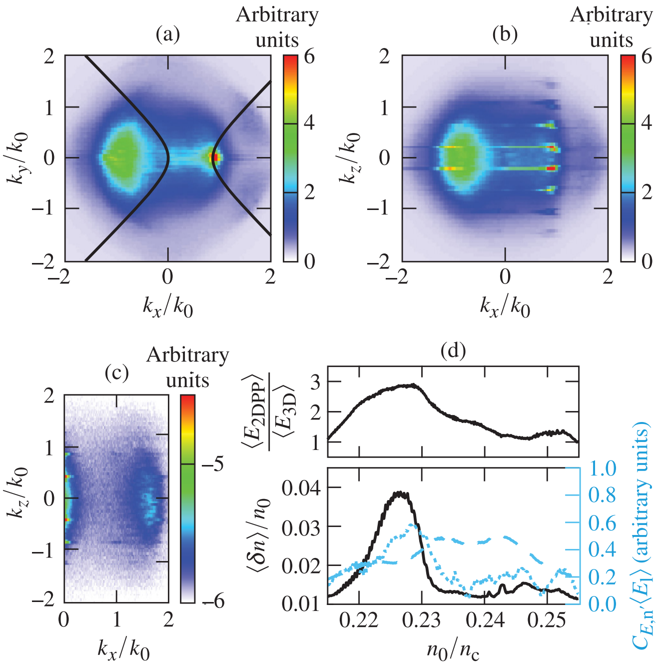

FIG. 4. (a) The spectrum of plasmons in the saturation stage of 3D simulation at densities lower than $0.23n_c$ plotted in the k_x-k_y plane and (b) the k_x-k_z plane. (c) The spectrum of ion density fluctuation plotted in the k_x-k_z plane on a logarithmic scale. (d) Lower panel: Ion density fluctuation rms (root-mean-square average over the transverse direction and time) normalized to background density (black solid line), longitudinal electric field rms (blue dashed line), and caviton correlator $C_{E,n}$ (blue dotted line). Upper panel: The ratio of the electric field amplitude of the TPD plasmons with a larger wave vector between 2D PP and 3D simulations.

vectors. Two types of low-frequency density fluctuations are identified in our simulations [see Fig. 4(c)]. One type are the ion acoustic waves driven by the Langmuir-decay instability (LDI) [17,18] and the other type are driven with the beating of the same-frequency daughter waves of SRS and TPD. The LDI modes form a broad feature at $k_x \approx 1.7k_0$ (about 2× the laser wave vector in plasma) in the spectrum of the ion density fluctuations shown in Fig. 4(c). The beating of the SRS plasmons with wave vector $(k_x, k_y, k_z) = (0.87k_0, 0, \pm 0.2k_0)$ creates density perturbations $\langle\delta n\rangle$ with wave vector $(k_x, k_z) = (0, \pm 0.4k_0)$. The coupling between SRS plasmons and $\langle\delta n\rangle$ generates higher-order modes in the field at $k_z = \pm(0.2 + m0.4k_0)$, [$m = 1, 2, \ldots$, see Fig. 4(b)] and in the density perturbation at $(k_x, k_z) = [0, \pm(0.4 + m0.4k_0)]$ [see Fig. 4(c)].

Although SRS and TPD grow independently in the linear stage, in the nonlinear stage they interact through low-frequency density perturbations. TPD growth starts from the region near $\frac{1}{4}n_c$ and spreads to lower densities [4]. Although the peak values of $\langle\delta n\rangle$ are similar in 2D and 3D simulations, the peaks are reached at different densities in different simulations: In 2D PP (without SRS) $\langle\delta n\rangle$ peaks at densities where absolute TPD modes dominate (around $0.245n_c$); in 3D (with both SRS and TPD) $\langle\delta n\rangle$ peaks at densities where the frequencies of TPD and SRS plasmons are close. In this region where the dispersion lines for TPD and SRS plasmons intersect [near $0.23n_c$ in our simulations, see Figs. 3(c) and 3(d)] multiple pairs of SRS and TPD daughter waves have close frequencies and can drive $\langle\delta n\rangle$ through the ponderomotive force to much higher levels compared to other density regions [see the black line in Fig. 4(d)]. The level of $\langle\delta n\rangle$ near $0.23n_c$ is lower in 2D PP than in 3D simulations. In the 3D simulation the growth of TPD plasmons at densities below $0.23n_c$, seeded by plasmons from above $0.23n_c$, is disrupted by these enhanced ion density perturbations, as illustrated by a decrease in the level of TPD-driven plasmons below $0.23n_c$ in Fig. 3(c).

The correlation between the local plasmon intensity $|E_L|^2$ and the density fluctuations δn is captured using the caviton correlator [5] $C_{E,n} = \langle -\delta n|E_L|^2\rangle/(\langle(\delta n)^2\rangle^{1/2}\langle|E_L|^2\rangle)$. As shown in the lower panel of Fig. 4(d), the plasma waves and the density fluctuations are weakly correlated between $0.255n_c$ and $0.235n_c$: $C_{E,n} = 0.1$–0.2 in spite of a significant level of plasmons in this density range. At densities close to $0.23n_c$, the lower panel of Fig. 4(d) shows the increase not only in the plasmon intensity and density fluctuations, but also in the correlation between them with $C_{E,n}$ reaching up to 0.6. The large caviton correlator indicates that the plasma waves are strongest in areas where density is depleted. The ponderomotive force of multiple pairs of SRS and TPD daughter waves with close frequencies is responsible for driving the enhanced density perturbations. The nonlinear coupling of TPD and SRS through ion perturbations leads to a lower TPD saturation level in the 3D simulation compared to the 2D PP simulation, which is illustrated in the upper panel of Fig. 4(d).

The fast-electron flux is defined as the energy flux carried by electrons with kinetic energy above 55 keV leaving the simulation box minus the energy flux carried by the thermal electrons injected into the simulation region from the thermal boundaries (in the x direction). Information about the hot electrons is collected during the saturation stage in each

TABLE I. Fast-electron flux normalized to the incident laser energy flux.

Fast-electron flux	Forward/backward	
Collision package	On	Off
Plane-wave 2D PP	1.6%/1.3%	5.5%/3.8%
Plane-wave 2D SP	(<0.1%)/0.2%	(<0.1%)/0.5%
Speckle 2D PP	6.8%/1.7%	9.4%/3.8%
Speckle 2D SP	(<0.1%)/0.3%	(<0.1%)/0.7%
Speckle 3D	0.4%/0.3%	0.8%/0.5%

simulation for 0.5 ps. In the 3D simulation, the fast-electron flux associated with the forward- and backward-going hot electrons was found to be 1.7% and 0.8%, respectively. The plasma-wave spectrum in the 3D simulation corresponds to a smaller k-space domain than the spectrum in 2D PP, which makes the staged acceleration mechanism less efficient in 3D than in 2D and explains a smaller number of hot electrons in the 3D simulation compared to 2D PP (6.6% and 3.4% in the forward and backward direction, respectively). The influence of wave breaking on the fast-electron generation is small as the maximal electric field amplitude ($0.04m_e\omega_0c/e$) is below the wave-break limit ($0.1m_e\omega_0c/e$) [7].

The nonlinear regime including both TPD and SRS is also observed in simulations with the speckled laser beam [19,20] and electron-ion collision effects included. In PIC simulations with periodic boundary conditions, the limited-size simulation region effectively represents a much larger volume of plasmas and the single speckle in the simulation region mirrors itself in the transverse directions. A series of simulations has been performed to study how the speckles affect the generation of hot electrons. All parameters are the same as the simulations described previously except for the temperatures of electrons and ions being 1.5 times higher. The peak intensities in the laser speckles are 1.8×10^{15} W/cm^2 (twice of the average intensities). A collision package (CP) is available for the PIC code OSIRIS [21]. The main physics processes are observed to be the same in simulations with plane-wave beams and speckled beams.

The fast-electron flux values in simulations are listed in Table I for different incident laser beams as well as with CP turned on and off. By comparing the left and right columns of Table I, one can see that adding collisions can reduce the fast-electron flux by about 50% and in the case of plane-wave 2D PP simulation by almost 70%. Also note that the reduction of the fast-electron flux caused by collisions affects both the forward-going electrons and backward-going electrons since the collisional damping rate affects all the plasma waves. The fast-electron flux generated in 2D SP is much smaller than the fast-electron flux generated in 2D PP, which indicates that the plasma waves driven by TPD are the main source of the electron acceleration.

The hot-electron fraction observed in the ICF experiments on the OMEGA laser system does not exceed a few percent [15]. At the same time, in the previous PIC simulations of TPD in 2D, the hot-electron fraction was close to an order of magnitude larger than in the experiments. The 3D PIC simulations presented in this Rapid Communication produce the results for the hot-electron fraction that are close to the experimental levels.

The laser-plasma interaction near $\frac{1}{4}n_c$ determines the generation of fast electrons that are crucial for the performance of ICF targets. The fast-electron flux in simulations is found to be closely related to the plasma-wave spectra. The TPD-driven plasma waves with large wave vectors are very important for accelerating electrons. At the same time, the SRS-driven plasma waves are less effective in accelerating electrons. Therefore the modeling including the nonlinear coupling of TPD and SRS in 3D is the only way to correctly describe the generation of fast electrons in laser-driven ICF.

Our 3D PIC simulations have shown the large decrease (up to an order of magnitude) in the fast-electron flux compared to 2D TPD modeling. The reason is the nonlinear coupling between SRS and TPD which is especially pronounced at densities lower than and around $0.23n_c$. In this region plasma waves and growing density perturbations are localized in the same areas as illustrated by the caviton correlator. Enhanced density perturbations detune and weaken the TPD-driven plasmons effective in the fast-electron generation. In addition to the TPD suppression, the plasma-wave spectra in 3D simulations are much more narrow compared to the spectra in 2D TPD modeling. To conclude, 3D PIC simulations presented in this Rapid Communication fully model the laser-plasma interaction near $\frac{1}{4}n_c$ including SRS and TPD, and obtain the fast-electron fraction level close to experimental results, resolving the large discrepancy between ICF experiments and PIC simulations that existed for many years before.

This material is based upon work supported by the Department of Energy National Nuclear Security Administration under Award No. DE-NA0003856, the University of Rochester, and the New York State Energy Research and Development Authority. We also acknowledge the support by the DOE under Grant No. DE-SC0012316, and by the NSF under Grant No. PHY-1314734.

---

[1] R. S. Craxton, K. S. Anderson, T. R. Boehly, V. N. Goncharov, D. R. Harding, J. P. Knauer, R. L. McCrory, P. W. McKenty, D. D. Meyerhofer, J. F. Myatt *et al.*, Phys. Plasmas **22**, 110501 (2015).

[2] J. F. Myatt, J. Zhang, R. W. Short, A. V. Maximov, W. Seka, D. H. Froula, D. H. Edgell, D. T. Michel, I. V. Igumenshchev, D. E. Hinkel *et al.*, Phys. Plasmas **21**, 055501 (2014).

[3] R. Yan, A. V. Maximov, C. Ren, and F. S. Tsung, Phys. Rev. Lett. **103**, 175002 (2009).

[4] R. Yan, C. Ren, J. Li, A. V. Maximov, W. B. Mori, Z.-M. Sheng, and F. S. Tsung, Phys. Rev. Lett. **108**, 175002 (2012).

[5] H. X. Vu, D. F. DuBois, D. A. Russell, and J. F. Myatt, Phys. Plasmas **19**, 102708 (2012).

[6] H. X. Vu, D. F. DuBois, J. F. Myatt, and D. A. Russell, Phys. Plasmas **19**, 102703 (2012).

[7] T. P. Coffey, Phys. Fluids **14**, 1402 (1971).

[8] J. M. Dawson, Rev. Mod. Phys. **55**, 403 (1983).

[9] A. Simon, R. W. Short, E. A. Williams, and T. Dewandre, Phys. Fluids **26**, 3107 (1983).

[10] C. S. Liu, M. N. Rosenbluth, and R. B. White, Phys. Fluids **17**, 1211 (1974).

[11] B. B. Afeyan and E. A. Williams, Phys. Plasmas **4**, 3803 (1997).

[12] J. F. Drake and Y. C. Lee, Phys. Rev. Lett. **31**, 1197 (1973).

[13] B. B. Afeyan and E. A. Williams, Phys. Plasmas **4**, 3845 (1997).

[14] W. Seka, D. H. Edgell, J. F. Myatt, A. V. Maximov, R. W. Short, V. N. Goncharov, and H. A. Baldis, Phys. Plasmas **16**, 052701 (2009).

[15] D. T. Michel, A. V. Maximov, R. W. Short, J. A. Delettrez, D. Edgell, S. X. Hu, I. V. Igumenshchev, J. F. Myatt, A. A. Solodov, C. Stoeckl *et al.*, Phys. Plasmas **20**, 055703 (2013).

[16] J. Meyer and Y. Zhu, Phys. Rev. Lett. **71**, 2915 (1993).

[17] D. F. DuBois and M. V. Goldman, Phys. Rev. **164**, 207 (1967).

[18] D. F. DuBois, H. A. Rose, and D. A. Russell, Phys. Scr. T **63**, 16 (1996).

[19] Y. Kato, K. Mima, N. Miyanaga, S. Arinaga, Y. Kitagawa, M. Nakatsuka, and C. Yamanaka, Phys. Rev. Lett. **53**, 1057 (1984).

[20] S. Skupsky, R. W. Short, T. Kessler, R. S. Craxton, S. Letzring, and J. M. Soures, J. Appl. Phys. **66**, 3456 (1989).

[21] R. A. Fonseca, L. O. Silva, F. S. Tsung, V. K. Decyk, W. Lu, C. Ren, W. B. Mori, S. Deng, S. Lee, T. Katsouleas *et al.*, in *Computational Science – ICCS 2002*, edited by P. M. A. Sloot, C. J. K. Tan, J. J. Dongarra, and A. G. Goekstra, Lecture Notes in Computer Science Vol. 2331 (Springer, Berlin, 2002), p. 342.